

DC response of an interferometer topology with an L-shaped cavity: a tabletop study

Junlang Li,^{1,2,*} Jiehong Huang,^{3,*} Xinyao Guo,³ Haixing Miao,³ Yuchao Chen,² Xiaoman Huang,² Yuan Pan,² Chenjie Zhou,² Raffaele Flaminio,⁴ Jameson Graef Rollins,⁵ Bram Slagmolen,⁶ Fan Zhang,^{7,2,†} Teng Zhang,^{8,‡} and Mengyao Wang^{2,§}

¹*School of Physics and Technology, Wuhan University, Wuhan 430072, China*

²*School of Physics and Astronomy, Beijing Normal University, Beijing, 100875, China*

³*Frontier Science Center for Quantum Information,
Department of Physics, Tsinghua University, Beijing, 100084, China*

⁴*Laboratoire d'Annecy de Physique des Particules,*

CNRS/IN2P3 9 Chemin de Bellevue - BP110 74941, Annecy-le-Vieux, Annecy, France

⁵*LIGO Laboratory, California Institute of Technology, Pasadena, California 91125, USA*

⁶*OzGrav, Australian National University, Canberra, Australian Capital Territory 0200, Australia*

⁷*Institute for Frontiers in Astronomy and Astrophysics,*

Beijing Normal University, Beijing 102206, China

⁸*School of Physics and Astronomy, University of Birmingham, Birmingham, B15 2TT, United Kingdom*

(Dated: January 16, 2026)

A new interferometer topology for kilohertz gravitational-wave detection was recently proposed in [Zhang *et al.* Phys. Rev. X 13, 021019 (2023)]. The design is based on an L-shaped optical cavity pumped through a Sagnac-like vortex. We report a tabletop experiment that characterizes the interferometer's optical response near DC. When the laser frequency is locked to the resonance of the L-shaped cavity, we observe that the cavity input coupler becomes effectively transparent, yielding a simple Michelson-like response. Moreover, the Sagnac vortex separates into upper and lower paths, which behave as two independent pumping paths driving the cavity. These observations are in agreement with theoretical predictions. Our results provide an intuitive physical picture of this interferometer topology and offer insight into its lock acquisition strategy.

I. INTRODUCTION

Gravitational-wave (GW) astronomy has progressed rapidly since the first detections by ground-based detectors [1–5], offering unprecedented insights into compact-object mergers and the physics of dense matter. In particular, the joint electromagnetic and GW observation of GW170817 event inaugurated the era of multi-messenger astronomy. Due to limited sensitivity of current detectors in the kilohertz regime, the (post-)merger GW signal from colliding neutron stars was not confidently confirmed because the detector noise is dominated at high frequencies by quantum noise originated from the quantum fluctuation of light [6–8]. Several quantum-enhanced schemes have been proposed to modify the input-output optics of the Michelson configuration to improve kHz sensitivity [9–12]. However, in the conventional Fabry-Perot Michelson configuration, the high-frequency signals are averaged out by the arm cavity response, and even small optical loss in the signal-recycling cavity will introduce additional vacuum noise that severely contaminates the high-frequency signals [13]. This imposes a quantum-loss limit of sensitivity at kHz frequency, and cannot be mitigated by simply increasing the arm length due to decreases of the arm cavity bandwidth.

A recently proposed alternative solution is to replace the linear arm cavities with a folded L-shaped optical cavity [14], similar to the Fox-Smith and synchronous interferometer [15–17]. By matching the temporal and spatial variation of the GW signal, this topology directly amplifies the kilohertz response at the free spectral range, and becomes immune to the loss in the signal recycling cavity. Its defining feature is an L-shaped cavity pumped through a Sagnac-like vortex, as depicted in Fig. 1. This topology requires a sensing and control scheme distinct from that used in current Michelson configuration. A preliminary attempt has been reported in Ref. [18], which combines the frontal modulation and an auxiliary control field injected from the dark port to obtain control signals for the core degrees of freedom. A critical step for implementing such a scheme is the development of a robust lock-acquisition procedure [19–21], which in turn requires both theoretical modeling and an intuitive understanding of the optical response of the core degrees of freedom.

Idealized theoretical analysis predicts that, when the end mirrors of the L-shaped cavity are perfectly reflective, the Sagnac-vortex behaves like that of a simple Michelson interferometer; if the laser frequency is locked to the resonance of the cavity, scanning the differential arm length will lead to a Michelson-like optical response. To validate this prediction, we perform a tabletop experiment to study the DC response of the interferometer topology, focusing on the common and differential modes within the region enclosed by the dashed box in Fig. 1. Our results confirm this simplified theoretical picture and reveal additional features relevant for control and prac-

* These authors contributed equally to this work.

† fnzhang@bnu.edu.cn

‡ tzhang@star.sr.bham.ac.uk

§ mengyao.wang@bnu.edu.cn

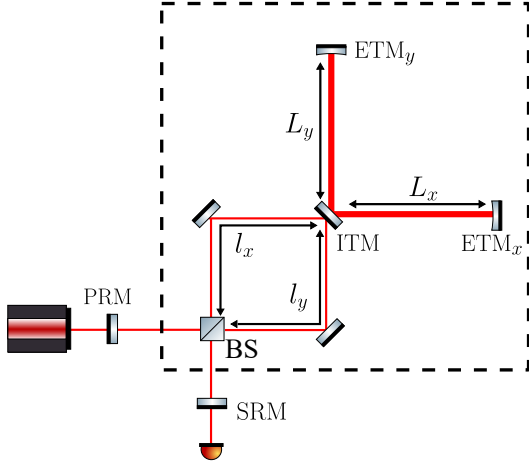


FIG. 1. Layout of the new topology with an L-shaped cavity and Sagnac-like vortex. BS:beam splitter; PRM: power recycling mirror; SRM: signal recycling mirror; ITM: input test mass; ETM: end test mass. The part enclosed by the dashed black box is the focus of the experimental study.

tical implementation.

This paper goes as follows. Section II presents the theoretical analysis of the new topology DC optical response. Section III describes the experimental setup and compares the measured results with the model. We conclude and discuss broader implications in Sec. IV.

II. THEORETICAL DESCRIPTION

In this section, we provide a more detailed description of the interferometer topology and derive the theoretical prediction of its DC optical response. As illustrated in Fig. 1, the input laser beam is split by the beamsplitter into two paths that circulate in opposite directions within the Sagnac vortex. We denote the clockwise path by x , with length of l_x and the counterclockwise path by y , with length l_y . The two arms of the L-shaped cavity have lengths L_x and L_y , respectively. Within this configuration, four longitudinal degrees of freedom can be identified: the Sagnac common mode ($l_+ = l_x + l_y$), the Sagnac differential mode ($l_- = l_x - l_y$), the L-shaped cavity common mode ($L_+ = L_x + L_y$), and the L-shaped cavity differential mode ($L_- = L_x - L_y$). As depicted in the left panel of Fig. 2a, the laser beam entering the L-shaped cavity for the x path (similarly, for the y path) is reflected in three ways, denoted as ①, ②, and ③. Specifically, ① corresponds to the prompt reflection by the L-shaped cavity without entering it, whereas ② and ③ represent the portions of field that enter the cavity and return from different directions.

We first analyze the ideal case in which both ETMs have perfect reflectivity ($r_e = 1$). When the cavity common mode L_+ is locked to resonance, the effective reflection coefficients of the L-shaped cavity for the three parts of each incident field can be derived as (see the Appendix

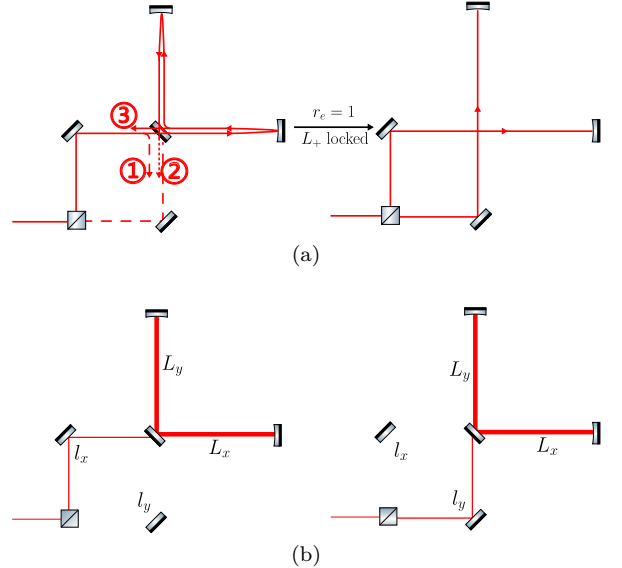


FIG. 2. (a) Schematic showing that the interferometer with an L-shaped cavity can be regarded as equivalent to a Michelson interferometer. The left panel of the figure only illustrates the circulation of the clockwise incident beam within the L-shaped cavity. The counterclockwise incident beam, indicated by the dashed line, has a symmetric circulation inside the cavity that is not shown. (b) Schematic showing that the input laser can be equivalent to two in-phase beams injected into the interferometer, traveling along the clockwise and counterclockwise paths of the Sagnac vortex, separately, and subsequently pump the L-shaped cavity from opposite directions.

for more details):

$$r_{xy} = r_{yx} = 0, \quad (1)$$

$$r_{xx} = e^{i \frac{2\omega_0 L_x}{c}}, \quad r_{yy} = e^{i \frac{2\omega_0 L_y}{c}}, \quad (2)$$

where the first subscript labels the input path and the second labels the output path. Equation (1) implies that the prompt reflection ① cancels exactly with ②. From Eqs. (1) and (2), each beam entering the L-shaped cavity is therefore completely reflected back along its incident direction. Consequently, when viewed from outside the cavity, the behavior of the beams that enter the L-shaped cavity and return is equivalent to that of beams propagating through the lengths L_x and L_y and being directly reflected by a mirror, since in both cases the reflected fields possess identical amplitudes and phases. The entire interferometer thus behaves effectively as a folded Michelson interferometer, as illustrated in the right panel of Fig. 2a. The corresponding DC powers at the dark and bright ports are then given by

$$\frac{S_{\text{dark}}}{S_{\text{in}}} = \sin^2 \left(\frac{\omega_0 \mathcal{L}_-}{c} \right), \quad \frac{S_{\text{bright}}}{S_{\text{in}}} = \cos^2 \left(\frac{\omega_0 \mathcal{L}_-}{c} \right), \quad (3)$$

where $\mathcal{L}_- = L_- + l_-$. Only the sum of L_- and l_- appears and it indicates the degeneracy of the two differential degrees of freedom. This interesting feature was also iden-

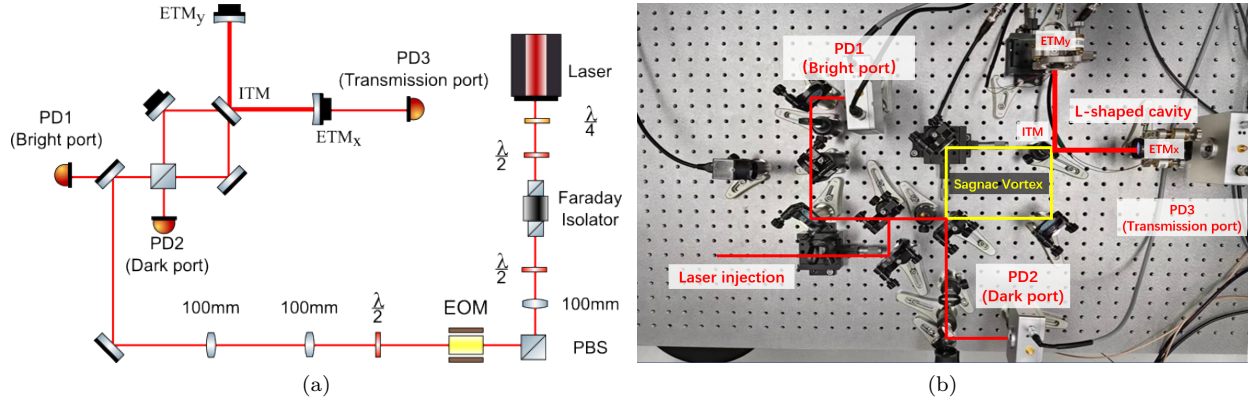


FIG. 3. Optical layout (a) and setup (b) of the experiment. The L-shaped interferometer contains two main parts, the Sagnac vortex and the L-shaped optical cavity. PBS: polarization beam splitter; EOM: electro-optic modulator; PD: photodetector.

tified in Ref. [18] when designing the sensing and control scheme.

Equation (1) also indicates that the Sagnac vortex effectively turns into two independent pumping paths as shown in Fig. 2b. The analytical expression for the intra-cavity power clearly reflects this feature:

$$\frac{S_{\text{cavity}}}{S_{\text{in}}} = \frac{1}{2t_i^2} \left| 1 + r_i e^{i \frac{\omega_0 \mathcal{L}_-}{c}} \right|^2, \quad (4)$$

where r_i and t_i denote the reflectivity and transmissivity of the ITM. This expression shows how the intra-cavity power varies as the two paths interfere with each other according to the differential phase difference. Comparing Eq. (4) with Eq. (3), we see that the period of the dark- and bright-port DC signals with respect to \mathcal{L}_- is twice that of the intra-cavity power. This can be understood intuitively as follows. Laser power within arm cavity is coherently pumped by two beams, as illustrated in Fig. 2b. When the common mode is locked, each beam is individually resonant in the L-shaped cavity, and the dependence of the circulating power on \mathcal{L}_- originates from the interference between the two beams. Regardless of the choice of phase reference within the cavity, the relative phase difference between the beams is determined by the single-trip phase difference accumulated along the clockwise and counterclockwise paths, which is equal to half of the round-trip phase difference between the two paths that could be observed at the dark port.

The above discussion assumes $r_e = 1$. In practice, ETMs have finite transmission ($r_e < 1$). In this case, even with L_+ locked, parts ① and ② no longer cancel with each other perfectly. Equation (1) is therefore modified to

$$r_{xy} = r_{yx} = -r_i + \frac{t_i^2 r_i r_e^2}{1 - r_i^2 r_e^2} \neq 0, \quad (5)$$

where the first term corresponds to ① and the second to ②. The full interferometer response can thus be separated into two modes: a Michelson mode, defined by

r_{xx} and r_{yy} , and a Sagnac mode defined by r_{xy} and r_{yx} , which behave like the beams in a Sagnac interferometer. At the dark port, the Sagnac-mode reflections from the two paths cancel perfectly, so the DC signal remains a sine function. At the bright port, however, the Sagnac mode contributes a constant offset because it is insensitive to variations in \mathcal{L}_- . As a result, the DC signal at the bright port exhibits a sinusoidal variation with a period of $\lambda/2$, while the amplitudes of the peaks are modulated by an additional cosine term with a period of λ . This picture is indeed followed from the more rigorous analysis, which modifies Eqs. (3) and (4) into

$$\frac{S_{\text{dark}}}{S_{\text{in}}} = \frac{t_i^4 r_e^2}{(1 - r_i^2 r_e^2)^2} \sin^2 \left(\frac{\omega_0 \mathcal{L}_-}{c} \right), \quad (6)$$

$$\frac{S_{\text{bright}}}{S_{\text{in}}} = \left| -\frac{t_i^2 r_e}{1 - r_i^2 r_e^2} \cos \left(\frac{\omega_0 \mathcal{L}_-}{c} \right) + \frac{r_i - r_i r_e^2}{1 - r_i^2 r_e^2} \right|^2, \quad (7)$$

$$\frac{S_{\text{cavity}}}{S_{\text{in}}} = \frac{t_i^2}{2(1 - r_i^2 r_e^2)^2} \left(1 + r_i^2 r_e^2 + 2r_i r_e \cos \left(\frac{\omega_0 \mathcal{L}_-}{c} \right) \right). \quad (8)$$

III. THE EXPERIMENTAL STUDY

In this section, we describe the tabletop experimental setup and compare the measured results with the theoretical predictions presented above.

The optical configuration of the setup is depicted schematically in Fig. 3a, and the physical layout of the core interferometer is shown in Fig. 3b. Laser first passes through a Faraday isolator to prevent back-reflections. It then traverses a half-wave plate and a polarization beam splitter, which together regulate the injection power. The beam is subsequently phase modulated by an electro-optic modulator (EOM) to generate the control sidebands required for the Pound–Drever–Hall locking scheme [22].

A third half-wave plate rotates the polarization from s- to p-polarization to match the preferred polarization of the L-shaped cavity. The beam is then mode-matched to the optical cavity using two 100 mm focal-length lenses. Two steering mirrors direct the beam into the interferometer; one of them is a 90% reflective beam splitter used to pick off the bright-port signal, which is collected by PD1. Two additional photodetectors, PD2 and PD3, monitor the DC power at the dark-port and the cavity transmission, respectively.

The common mode L_+ of the L-shaped cavity is controlled by synchronously actuating the two ETMs using piezoelectric actuators. Once L_+ is locked to the laser frequency, the differential mode L_- can be scanned either by modulating the steering mirror in the Sagnac loop l_- or by differentially actuating the two ETMs L_- , consistent with the degeneracy in Eq. (3). In the experiment, we adopt the former approach by applying a ramp signal to the piezoelectric actuator of the Sagnac steering mirror. During the scan, the corresponding DC powers at all three ports were recorded in real time.

For quantitative comparison with the theoretical model, the following calibration procedures were performed. Firstly, the photodetector signals were converted to optical power, taking into account variations in detector responsivity and the optical transmission factors. Secondly, the piezoelectric actuator response was independently calibrated, and its intrinsic nonlinearity was corrected. This procedure linearized the scan, enabling a direct conversion of the actuator drive voltage to an equivalent physical displacement. Finally, the calibrated signals from the photodetectors were fitted simultaneously to the analytic expressions in Eqs. (6) - (8), which describe the dependence of the bright-port, dark-port, and transmission port powers on the differential length. Figure 4 shows the calibrated data overlaid with the best-fit theoretical curves. We have used two fitting parameters: the reflectivities of the ITM and ETM. The best-fit values, $R_{\text{ITM}} = 97.8\%$ and $R_{\text{ETM}} = 99.7\%$, agree well with the specifications from the optics vendor.

There are overall offsets observed in the bright-port and dark-port signals, which were not covered by the idealized theoretical model. The model predicts that all three DC signals should reach zero at specific values of the differential length. This deviation arises because the analytical derivation assumes ideal plane-wave propagation and neglects higher-order transverse modes. In practice, residual mode mismatch and imperfect alignment introduce contrast defects at the output ports that lead to nonzero offsets. To assess the impact of mode mismatch more quantitatively, we have carried out a numerical simulation using Finesse [23]. We found a mode mismatch of order of 4% is sufficient to reproduce the observed offsets, which agrees with the difference between the measured beam waist near ITM and the value expected from the cavity geometry. The full set of experimental parameters is summarized in Table I.

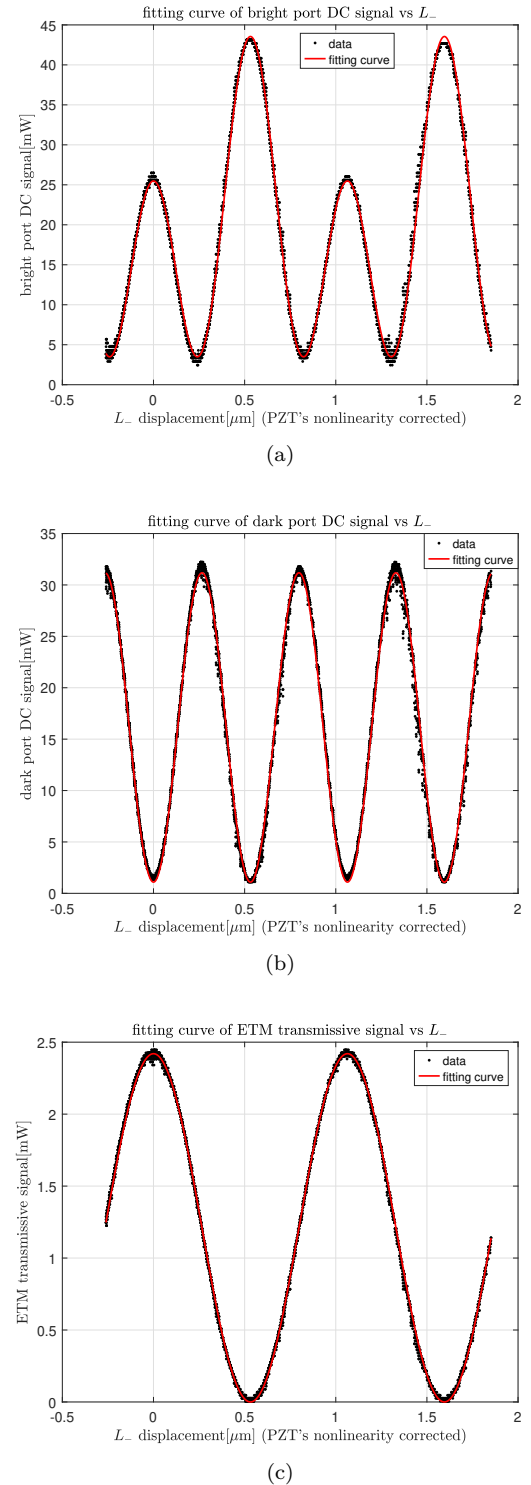


FIG. 4. Measured output power at the (a) bright, (b) dark, and (c) transmission ports. Data were fitted based on Eqs. (6)-(8), yielding reflectivities of $R_i = 97.8\%$ for the ITM and $R_e = 99.7\%$ for two ETMs.

Parameter	Value
EOM modulation frequency	15 MHz
EOM modulation depth	0.15 rad
cavity arm common mode L_+	20.3 cm
cavity arm differential mode L_-	0.1 cm
Sagnac common mode l_+	46.3 cm
Sagnac differential mode l_-	0.3 cm
ITM reflection R_i	97.8%
ETM reflection R_e	99.7%
ETM radius of curvature	1 m
ideal beam waist radius at ITM	318.8 μ m
measured beam waist radius at ITM	304.5 μ m
beam waist radius mismatch	14.3 μ m
beam waist position mismatch	11.1 cm
mode mismatch at ITM	3.85%

TABLE I. Parameters of the experiment. The reflection of the mode mismatch is given directly by Finesse.

IV. CONCLUSION

In this work, we have investigated the DC optical response of the recently proposed L-shaped cavity interferometer topology for kilohertz gravitational-wave detection. Through a controlled tabletop experiment, we verified two key theoretical predictions: (i) when the laser is locked to the resonance of the L-shaped cavity, the prompt and first-pass reflection cancel in such a way that the cavity input coupler becomes effectively transparent, and the interferometer with an L-shaped cavity behaves as a folded Michelson; and (ii) the Sagnac vortex decomposes into two independent pumping paths whose interference governs both the intra-cavity power

and the output-port signals. The experimental results, obtained through calibrated scans of the differential degree of freedom, show nice agreement with the analytic and numerical model. The intuitive physical picture developed here—namely, the transparent-ITM behavior at resonance, the degeneracy between the cavity and Sagnac differential modes, and the two-path pumping interpretation—helps clarify the lock-acquisition pathways and the structure of error signals available for stabilizing the interferometer in its target operating state.

Looking forward, these results form a stepping stone toward implementing this topology in larger-scale prototypes, e.g., the one under construction at Beijing Normal University [24], realizing a suspended interferometer with the L-shaped cavity. In the longer term, the insights developed here support the broader program of engineering next-generation kHz gravitational-wave detectors capable of probing neutron-star post-merger oscillations. As the L-shaped cavity topology is further integrated with squeezed-light injection, high-power operation, and low-loss optical coatings, the combination of theoretical modeling, tabletop validation, and intermediate-scale prototypes will help assess its viability for future observatories.

V. ACKNOWLEDGE

This work was supported by the National Key Research and Development Program of China (Grant Nos. 2024YFC2208000, and 2023YFC2205800), the National Natural Science Foundation of China (Grant Nos. 12441503 and 12433001), the Fundamental Research Funds for the Central Universities of China(Grant No. 310432103). We also acknowledge the support of the Institute for Gravitational Wave Astronomy at the University of Birmingham, UK.

[1] B. P. Abbott, R. Abbott, et al. Observation of gravitational waves from a binary black hole merger. *Phys. Rev. Lett.*, 116:061102, Feb 2016.

[2] B. P. Abbott, R. Abbott, et al. Gw170817: Observation of gravitational waves from a binary neutron star inspiral. *Phys. Rev. Lett.*, 119:161101, Oct 2017.

[3] The LIGO Scientific Collaboration, J Aasi, et al. Advanced ligo. *Classical and Quantum Gravity*, 32(7):074001, mar 2015.

[4] R. Abbott, T. D. Abbott, et al. GWTC-3: Compact Binary Coalescences Observed by LIGO and Virgo during the Second Part of the Third Observing Run. *Physical Review X*, 13(4):041039, October 2023.

[5] A. G. Abac, I. Abouelfettouh, et al. Gwtc-4.0: An introduction to version 4.0 of the gravitational-wave transient catalog. *The Astrophysical Journal Letters*, 995(1):L18, dec 2025.

[6] Yanbei Chen. Macroscopic quantum mechanics: theory and experimental concepts of optomechanics. *Journal of Physics B: Atomic, Molecular and Optical Physics*, 46(10):104001, may 2013.

[7] Rana X. Adhikari. Gravitational radiation detection with laser interferometry. *Rev. Mod. Phys.*, 86:121–151, Feb 2014.

[8] Stefan L. Danilishin, Farid Ya. Khalili, and Haixing Miao. Advanced quantum techniques for future gravitational-wave detectors. *Living Reviews in Relativity*, 22(1):2, 2019.

[9] Haixing Miao, Huan Yang, and Denis Martynov. Towards the design of gravitational-wave detectors for probing neutron-star physics. *Phys. Rev. D*, 98:044044, Aug 2018.

[10] Denis Martynov, Haixing Miao, et al. Exploring the sensitivity of gravitational wave detectors to neutron star physics. *Phys. Rev. D*, 99:102004, May 2019.

[11] K. Ackley, V. B. Adya, et al. Neutron star extreme matter observatory: A kilohertz-band gravitational-wave detector in the global network. *Publications of the Astronomical Society of Australia*, 37:e047, 2020.

[12] LSC membeber. Report of the lsc post-o5. *LIGO Technical notes-T2200287*, 2023.

[13] Haixing Miao, Nicolas D. Smith, and Matthew Evans. Quantum limit for laser interferometric gravitational-

wave detectors from optical dissipation. *Phys. Rev. X*, 9:011053, Mar 2019.

[14] Teng Zhang, Huan Yang, et al. Gravitational-wave detector for postmerger neutron stars: Beyond the quantum loss limit of the fabry-perot-michelson interferometer. *Phys. Rev. X*, 13:021019, May 2023.

[15] P. Smith. Stabilized, single-frequency output from a long laser cavity. *IEEE Journal of Quantum Electronics*, 1(8):343–348, 1965.

[16] R. W. Drever. Interferometric detectors for gravitational radiation. *Lect. Notes Phys.* 124, 321, 1983.

[17] Jean-Yves Vinet, Brian Meers, et al. Optimization of long-baseline optical interferometers for gravitational-wave detection. *Phys. Rev. D*, 38:433–447, Jul 1988.

[18] Xinyao Guo, Teng Zhang, et al. Sensing and control scheme for the interferometer configuration with an l-shaped resonator. *Classical and Quantum Gravity*, 40(23):235005, oct 2023.

[19] Matthew Evans. *Lock Acquisition in Resonant Optical Interferometers*. PhD thesis, California Institute of Technology, 2002.

[20] Denis Martynov. *Lock Acquisition and Sensitivity Analysis of Advanced LIGO Interferometers*. PhD thesis, California Institute of Technology, 2015.

[21] A Staley, D Martynov, et al. Achieving resonance in the advanced ligo gravitational-wave interferometer. *Classical and Quantum Gravity*, 31(24):245010, nov 2014.

[22] Eric D. Black. An introduction to pound-drever-hall laser frequency stabilization. *American Journal of Physics*, 69:79–87, 2001.

[23] Daniel David Brown, Andreas Freise, et al. Finesse, March 2025.

[24] Mengyao Wang, Fan Zhang, et al. Beijing normal university 12-meter interferometric khz gravitational wave detector prototype: Design and scientific prospects. *Science China Physics, Mechanics & Astronomy*, 69(3):239511, 2026.

Appendix A: Derivation of each readout

Here we provide the derivation of Eqs. 1–8. With the notation in Fig. 2, the reflected field of the beam propagating through the clockwise path and returning along the same path, namely portion ③ in the figure, is expressed as $r_{xx}E_{\text{in}}$, where E_{in} denotes the incident field and r_{xx} is the corresponding reflectivity. The first subscript indicates the incident path, and the second represents the returning path. Similarly, r_{yy} corresponds to the reflection of the beam impinging and returning along the counterclockwise path.

Hence, the effective reflectivities of the L-shaped cavity for the two incident paths can be written as

$$r_{xx} = -\frac{t_i^2 r_e e^{i\frac{2\omega L_x}{c}}}{1 - r_i^2 r_e^2 e^{i2\phi}}, \quad r_{yy} = -\frac{t_i^2 r_e e^{i\frac{2\omega L_y}{c}}}{1 - r_i^2 r_e^2 e^{i2\phi}}, \quad (\text{A1})$$

and

$$r_{yx} = r_{xy} = r_i - \frac{t_i^2 r_i r_e^2 e^{i2\phi}}{1 - r_i^2 r_e^2 e^{i2\phi}} = \frac{r_i - r_i r_e^2 e^{i2\phi}}{1 - r_i^2 r_e^2 e^{i2\phi}}. \quad (\text{A2})$$

Here r_i and r_e denote the reflectivities of the input and end test masses (ITM and ETM) of the L-shaped cavity, respectively. The total phase is defined as $\phi = \omega L_+/c$, where L_+ is the L-shaped cavity common mode. The frequency ω may correspond to either the carrier ω_0 or $\omega_0 \pm \omega_m$, where ω_m is the modulation frequency of the radio-frequency (RF) sidebands, since both the carrier and the RF sidebands share the same functional form of effective reflectivity.

For carrier, when L_+ is locked at resonance, there is $e^{i\phi} = 1$, and the subsequent analysis is based on this condition. In the ideal case where $r_e = 1$, Eqs. (A1)–(A2) yield $r_{xy} = r_{yx} = 0$, meaning that light entering from the x path returns entirely through the same path, and likewise for the y path. This is the derivation of Eqs. 1 and 2. The interferometer therefore becomes equivalent to a folded Michelson interferometer when viewed from outside the L-shaped cavity. When $r_e < 1$, however, r_{xy} and r_{yx} are nonzero; these components are referred to as the Sagnac mode, and $r_{xy} = r_{yx}$ always holds.

Consequently, the overall reflectivity of the interferometer for light input and output from the bright port is given by

$$\begin{aligned} r_{br} &= \frac{1}{2}(e^{i2\psi_1}r_{xx} + e^{i(\psi_1+\psi_2)}r_{xy} + e^{i(\psi_1+\psi_2)}r_{yx} + e^{i2\psi_2}r_{yy}) \\ &= -\frac{t_i^2 r_e e^{i\phi}}{1 - r_i^2 r_e^2 e^{i2\phi}} \cos\left(\frac{\omega L_-}{c}\right) + \frac{r_i - r_i r_e^2 e^{i2\phi}}{1 - r_i^2 r_e^2 e^{i2\phi}}, \end{aligned} \quad (\text{A3})$$

and the corresponding transmission to the dark port is

$$\begin{aligned} t_{dr} &= \frac{1}{2}(e^{i2\psi_1}r_{xx} - e^{i(\psi_1+\psi_2)}r_{xy} + e^{i(\psi_1+\psi_2)}r_{yx} - e^{i2\psi_2}r_{yy}) \\ &= i2e^{i(\psi_1+\psi_2)} \frac{t_i^2 r_e e^{i\phi}}{1 - r_i^2 r_e^2 e^{i2\phi}} \sin\left(\frac{\omega L_-}{c}\right), \end{aligned} \quad (\text{A4})$$

where $L_- = L_+ + l_-$, $\psi_1 = \omega l_x/c$, $\psi_2 = \omega l_y/c$ and ω applies to both the carrier and the RF sidebands.

Even in the presence of the Sagnac mode, the DC signal at the dark port remains a purely sinusoidal function, which is the characteristic of a Michelson-like interferometer. The DC signal at the dark port is therefore expressed as

$$\begin{aligned} \frac{S_{\text{dark}}}{S_{\text{in}}} &= J_0^2 |t_{dr,c}|^2 + J_1^2 (|t_{dr,s+}|^2 + |t_{dr,s-}|^2) \\ &\approx \frac{t_i^4 r_e^2}{(1 - r_i^2 r_e^2)^2} \sin^2\left(\frac{\omega_0 L_-}{c}\right), \end{aligned} \quad (\text{A5})$$

where S_{in} is the input optical power, and $t_{dr,c}$, $t_{dr,s+}$, and $t_{dr,s-}$ are the transmissions of the carrier and the upper and lower sidebands, respectively. In our experiment, the modulation depth is quite small such that $J_1 \ll J_0$. Consequently, when considering the DC signal, the sideband contribution can be safely neglected, which leads to Eq. 6.

Similarly, the DC signal at the bright port is given by

$$\begin{aligned} \frac{S_{\text{bright}}}{S_{\text{in}}} &= J_0^2 |r_{br,c}|^2 + J_1^2 (|r_{br,s+}|^2 + |r_{br,s-}|^2) \\ &\approx \left| -\frac{t_i^2 r_e}{1 - r_i^2 r_e^2} \cos\left(\frac{\omega_0 \mathcal{L}_-}{c}\right) + \frac{r_i - r_i r_e^2}{1 - r_i^2 r_e^2} \right|^2, \end{aligned} \quad (\text{A6})$$

which corresponds to Eq. 7. Expanding the expression yields

$$\begin{aligned} \frac{S_{\text{bright}}}{S_{\text{in}}} &= \frac{t_i^4 r_e^2}{(1 - r_i^2 r_e^2)^2} \cos^2\left(\frac{\omega_0 \mathcal{L}_-}{c}\right) \\ &\quad - 2 \frac{t_i^2 t_e^2 r_i r_e}{(1 - r_i^2 r_e^2)^2} \cos\left(\frac{\omega_0 \mathcal{L}_-}{c}\right) + \frac{r_i^2 t_e^4}{(1 - r_i^2 r_e^2)^2}. \end{aligned} \quad (\text{A7})$$

It can be seen that the bright-port signal contains both first- and second-order cosine terms; therefore, the peak spacing corresponds to $\lambda/2$, while the amplitude modulation has a period of λ .

Following the same procedure, the transmission coefficients from outside into the L-shaped cavity through the

ITM can be written as

$$t_{xx} = \frac{t_i e^{i \frac{\omega L_x}{c}}}{1 - r_i^2 r_e^2 e^{i 2\phi}}, \quad t_{yx} = \frac{t_i e^{i \frac{\omega L_y}{c}} r_i r_e e^{i \phi}}{1 - r_i^2 r_e^2 e^{i 2\phi}}. \quad (\text{A8})$$

t_{xx} represents the transmission of light incident from the x path into the x arm of the L-shaped cavity, while t_{yx} represents the transmission of light incident from the y path into the x arm of the L-shaped cavity. Besides, the sidebands are off-resonance in the cavity. Thus, the total power in the L-shaped cavity is given by

$$\begin{aligned} \frac{S_{\text{cavity}}}{S_{\text{in}}} &= \frac{1}{2} \left| e^{i \frac{\omega_0 t_x}{c}} t_{xx} + e^{i \frac{\omega_0 t_y}{c}} t_{yx} \right|^2 \\ &= \frac{t_i^2}{2(1 - r_i^2 r_e^2)^2} \left(1 + r_i^2 r_e^2 + 2 r_i r_e \cos\left(\frac{\omega_0 \mathcal{L}_-}{c}\right) \right), \end{aligned} \quad (\text{A9})$$

which corresponds to Eq. 8. In experiment, we extract the intra-cavity power from one of the ETM transmission port, whose power is $S_{\text{trans}} = t_e^2 S_{\text{cavity}}$. Since, for $r_e = 1$, Eqs. 6-8 degenerate to Eqs. 3-4, no additional proof is required. It is also straightforward to verify that if both ETMs are lossless (namely $r_e^2 + t_e^2 = 1$), the relationship $S_{\text{bright}} + S_{\text{dark}} + 2S_{\text{trans}} = 1$ holds, which satisfies energy conservation and confirms the validity of the theoretical model.